# On the study of Structural properties and Cation distribution of $Zn_{0.75-x}Ni_xMg_{0.15}Cu_{0.1}Fe_2O_4$ nano ferrite: Effect of Ni addition

**M Satalkar[a], S N Kane[a,1]**
[a]Magnetic Materials Laboratory, School of Physics, D. A. University, Khandwa road, Indore-452001, India

E-mail: kane_sn@yahoo.com (S. N. Kane)

**Abstract.** Effect of Ni addition on structural properties and, cation distribution of $Zn_{0.75-x}Ni_xMg_{0.15}Cu_{0.1}Fe_2O_4$ (x = 0.0, 0.15, 0.30, 0.60, 0.75) ferrites, prepared using sol-gel auto-combustion method was studied using X-ray diffraction (XRD) technique. XRD analysis reveals the formation of spinel phase even in dry gel form. The lattice constant ($a_{exp.}$) decreases with $Ni^{2+}$ substitution and follows Vegard's law. Scherrer's grain diameter ($D$) lies within the range of 17.33 – 26.47 nm. Due to difference in the ionic radii of $Zn^{2+}$ and $Ni^{2+}$ significant changes are observed in the structural parameters - unit cell volume ($V$), hopping length at A ($L_A$) and B ($L_B$) site, and x-ray density ($\rho_{XRD}$). Linear increase in Neel magnetic moment ($n_B^N$) with oxygen positional parameter is observed in the studied samples, attributed to simultaneous weakening of A–B interaction and strengthening of the B–B interaction.

## 1. Introduction

Spinel ferrite, $MFe_2O_4$ (M = $Mn^{2+}$, $Co^{2+}$, $Zn^{2+}$, $Mg^{2+}$, etc.), is one of the most important magnetic oxides, where oxygen has fcc close packing and $M^{2+}$ and $Fe^{3+}$ ions occupy either tetrahedral (A) or octahedral (B) interstitial sites. The spinel ferrite is a very promising candidate for understanding and controlling the magnetic properties of nanoparticles at the atomic level. They are the most widely used structural material having low cost, high performance for high-frequency applications. Several methods, [1, 2] have been used to synthesize spinel ferrite nanoparticles. Among all these synthesis methods, sol-gel auto-combustion has been proved to be a simple and economic way to prepare nanoscale powders. In this technique, a thermally induced anionic redox reaction takes place. The energy from the exothermic reaction between oxidant and reductant can be high enough to form a spinel ferrite phase within a very short period of time i. e. even in dry gel/as-burnt form (i. e. the samples are without any thermal/sintering treatment). The literature also reports about the spinel phase formation in dry gel form in Cr doped Ni-Cu-Zn [3], Ni-Cu-Zn [4], Zn substituted in Mg-Ni ferrite [5], Ni doped Zn-Mg-Cu ferrite [6].

Substituted spinel ferrites with different divalent cations, are important candidate for both the fundamental studies and application point of view. Spinel ferrites are used in various applications, such as drug delivery [7] bio-separation, magnetic refrigeration systems [8], gas sensing [9], catalytic application [10], absorbent materials [11], ultra high density recording, magnetic resonance imaging, data processing devices, microwave and radio frequency devices, quantitative immunoassay [12], multilayer chip inductor and electromagnetic interference (EMI) suppression [13]. These applications of ferrites depend on its structural, magnetic and electrical properties. The origin of such properties of

spinel ferrites is attributed to the cations distribution among tetrahedrally coordinated A sites (8 per unit cell) and octahedrally coordinated B sites (16 per unit cell). In general, magnetic characteristics of spinel ferrites are largely governed by three types of anti-ferromagnetic superexchange interaction, namely, $J_{AA}$ (A–O–A), $J_{AB}$ (A–O–B), and $J_{BB}$ (B–O–B), between cations on the A and B sites, each mediated by oxygen ions. Among them, $J_{AB} >> J_{BB}$, whereas $J_{AA}$ is small due to the large separation between two A-site ions. Owing to the difference in the size of cations, any alteration in their distribution changes the lattice constant and the oxygen parameter, thereby altering spin interactions that determine $J_{AB}$.

According to authors best knowledge no literature is available which reports the cation distribution of as-burnt Zn-Ni-Mg-Cu ferrite. Bachhava, et al [14] studied similar composition: $Ni_xMg_{0.5-x}Cu_{0.1}Zn_{0.4}Fe_2O_4$ (x = 0.1, 0.2, 0.3, 0.4 and 0.5) annealed at 1050$^o$C for 24 hours and, observe decrease in the cation distribution parameters: bond lengths ($R_A$, $R_B$) and site radii ($r_A$, $r_B$) with nickel content. Although the above mentioned paper gives the parameters obtained by cation distribution, but does not report the obtained cation distribution for the studied system: $Ni_xMg_{0.5-x}Cu_{0.1}Zn_{0.4}Fe_2O_4$ ferrite [14]. Cation distribution can give an enhanced understanding of the magnetic interaction in spinel ferrites. Therefore, a clear understanding of the cation distribution in spinel ferrites is essential for studying and controlling their structural, magnetic properties [15] and to establish a better relationship between them so that the properties of spinel ferrite can be easily tuned just by varying the distribution of cations at A and B site.

Therefore, the present work focuses on the structural properties and, cation distribution of as-burnt $Zn_{0.75-x}Ni_xMg_{0.15}Cu_{0.1}Fe_2O_4$ (x = 0.00, 0.15, 0.30, 0.60, 0.75) powder synthesized via sol-gel auto-combustion method.

## 2. Experiment details

$Zn_{0.75-x}Ni_xMg_{0.15}Cu_{0.1}Fe_2O$ spinel ferrite powders with x = 0.00, 0.15, 0.30, 0.60, 0.75 were prepared by sol-gel auto-combustion technique. For the synthesis, citrate–nitrate/acetate pre-cursors [Zinc Nitrate – $Zn(NO_3)_2.6H_2O$, Nickel Acetate – $Ni(CH_3COO)_2.4H_2O$, Magnesium Acetate – $(CH_3COO)_2.Mg.4H_2O$, Copper Nitrate – $Cu(NO_3)_2.3H_2O$ and Ferric Nitrate – $Fe(NO_3)_3.9H_2O$] were mixed in stoichiometric ratio with citric acid as fuel. Metal salt to fuel ratio was taken as 1:1. All the pre-cursors were dissolved in de-ionized water to form aqueous solution. The pH value of solution was adjusted to 7 using ammonia ($NH_4OH$). Subsequently the aqueous solution was heated and evaporated under intensive stirring to transform into xerogel. The auto-combustion reaction was initiated by heating xerogel in air till the loose powder was formed called as 'dry gel or as-burnt powder' which was used for structural measurements.

## 3. Calculations

Experimental Lattice parameter ($a_{exp.}$) was determined using the relation - $a = d\sqrt{h^2 + k^2 + l^2}$, where d – inter-planer spacing and, (h, k, l) - miller indices. X-ray density ($\rho_{XRD}$) was obtained by [16]: $\rho_{XRD} = 8M_w / Na_{exp.}^3$, where $M_w$ – Molecular weight, N – Avagrado's Number. Scherrer's grain diameter ($D$) of the spinel powders was calculated from the x-ray broadening of the diffraction peak [311] using the Scherrer formula [17]: $D = 0.9\lambda / \beta \cos\theta$, where λ - wavelength of the x-ray used, β - line width, θ - peak position (in 2θ scale). The jump/hopping length '$L$' (the distance between the magnetic ions) for tetrahedral (A) and octahedral [B] site was calculated by using the expressions [18]: $L_A = (a_{exp.}\sqrt{3})/4$ and, $L_B = (a_{exp.}\sqrt{2})/4$, where $L_A$ and $L_B$ are respectively the hoping length for site A and site B. The specific surface area of the particles ($S$), which is the summation of the areas of the exposed surfaces of the particles per unit mass and is calculated by using the formula [19]: $S = 6/(D \times \rho_{XRD})$, where D = Scherre's grain diameter (nm) and $\rho_{XRD}$ = x-ray density (g/m$^3$).

Cation distribution in spinel ferrite can be obtained from the analysis of XRD pattern. In this work,

the Bertaut method [20] is used to determine the cation distribution. This method selects a few pairs of reflections according to the expression: $I_{hkl}^{obs} / I_{h'k'l'}^{obs} = I_{hkl}^{cal} / I_{h'k'l'}^{cal}$, where $I_{hkl}{}^{obs}$ and $I_{hkl}{}^{cal}$ are the observed and calculated intensities for reflection (hkl), respectively. Best information regarding cation distribution can be obtained on comparing experimental and calculated intensity ratios for reflections which does not depend of the oxygen positional parameter (*u*). In the present study, (220) (422) (400) (440) planes are considered for cation distribution as these planes are sensitive to distribution of cation among tetrahedral (A) and octahedral [B] sites of the spinel lattice. The calculated and observed intensity ratios were compared for several combinations of cations distribution at (A) and [B] sites as described in [21]. The best cation distribution among the tetrahedral and octahedral sites for which, theoretical and experimental intensities ratios agree clearly, is taken to be the correct one. Observed intensities of the planes: 220, 440 and 311 were used for the calculation of the orientation degree. The orientation degree of the hk0 ($\boldsymbol{O_{hk0}}$) and 220 ($\boldsymbol{O_{220}}$) plane was calculated by using the formula: $I_{220} + I_{440} / I_{311}$ and $I_{220} / I_{311}$ respectively [22].

With the help of obtained cation distribution, ionic radii of A-site ($\boldsymbol{r_A}$) and B-site ($\boldsymbol{r_B}$) can be calculated using the relations [23]:

$r_A = (C_{AMg}{}^{2+} \times r_{Mg}{}^{2+}) + (C_{ANi}{}^{2+} \times r_{Ni}{}^{2+}) + (C_{AZn}{}^{2+} \times r_{Zn}{}^{2+}) + (C_{ACu}{}^{2+} \times r_{Cu}{}^{2+}) + (C_{AFe}{}^{3+} \times r_{Fe}{}^{3+})$

$r_B = [(C_{B\,Mg}{}^{2+} \times r_{Mg}{}^{2+}) + (C_{BNi}{}^{2+} \times r_{Ni}{}^{2+}) + (C_{BZn}{}^{2+} \times r_{Zn}{}^{2+}) + (C_{BCu}{}^{2+} \times r_{BCu}{}^{2+}) + (C_{BFe}{}^{3+} \times r_{Fe}{}^{3+})]/2$

Where, $C_A$ and $C_B$ are respectively the ionic concentration at A and B sites, $r_{Mg}{}^{2+}$, $r_{Ni}{}^{2+}$, $r_{Zn}{}^{2+}$, $r_{Cu}{}^{2+}$, $r_{Fe}{}^{3+}$ are the ionic radius of $Mg^{2+}$, $Ni^{2+}$, $Zn^{2+}$, $Cu^{2+}$ and $Fe^{3+}$ respectively, which are taken from the work of Shannon [24]. Using the ionic radii of A-site ($r_A$) and B-site ($r_B$), theoretical lattice parameter ($a_{th}$) is calculated using the formula [23]: $a_{th} = (8/3\sqrt{3})\left[(r_A + R_0) + \sqrt{3}(r_B + R_0)\right]$, where $R_o$ is the ionic radius of oxygen ion - 0.138nm.

The spinel structure consists of cubic close packed arrangement (fcc) of $O^{2-}$ ions. Each unit cell contains eight formula units of $AB_2O_4$ with space group Fd3m. The location of the atoms in the spinel depends on the choice of origin in the Fd3m space group. The conventional choices for the origin in the spinel unit cell are either an A-site cation with $\bar{4}3m$ or an octahedral vacancy with $\bar{3}m$ [25]. Oxygen positional parameter or anion parameter (*u*), which is the distance between the oxygen ion and the face of the cube edge along the cube diagonal of the spinel lattice is calculated by [16] : $u^{\bar{4}3m} = ((r_a + R_o)/(\sqrt{3} * a_{exp})) + (1/4)$ (for the unit-cell origin at either $\bar{4}3m$ on an A-site cation ) and $u^{\bar{3}m} = u^{\bar{4}3m} - (1/8)$ (for the unit-cell origin at $\bar{3}m$ on an octahedral vacancy). Where, $r_A$ = ionic radii of A-site, $R_o$ = 0.138 nm (ionic radius of oxygen ion) and $a_{exp.}$ = experimental lattice parameter. For a perfect fcc structure, ideal oxygen positional parameter ($u_{ideal}$) for origin at $\bar{4}3m$ and $\bar{3}m$ respectively is $u_{ideal}{}^{\bar{4}3m} = 0.375$ and $u_{ideal}{}^{\bar{3}m} = 0.250$. In spinel ferrite the distances between the unshared anions (shared tetrahedral edge - $d_{AE}$) and shared anions (shared octahedral edge - $d_{BE}$) can also be calculated by using respective formula [25]: $d_{AE} = a_{exp.}\sqrt{2}\left(2u^{\bar{4}3m} - 0.5\right)$ and $d_{BE} = a_{exp.}\sqrt{2}\left(1 - 2u^{\bar{4}3m}\right)$. The distance between the tetrahedral cation and anion, known as tetrahedral bond length ($R_A$) and the distance between the octahedral cation and anion, known as octahedral bond length ($R_B$) was calculated by using the expressions [25]: $R_A = a_{exp.}\sqrt{3}\left(u^{\bar{4}3m} - (1/4)\right)$ and, $R_B = a_{exp.}\sqrt{3\left(u^{\bar{4}3m}\right)^2 - (11/4)u^{\bar{4}3m} + (43/64)}$. The interionic distances between cations ($M_e$-$M_e$) (*b, c, d, e, f)* was calculated using the formula: $b = (a_{exp.}/4)\sqrt{2}$, $c = (a_{exp.}/8)\sqrt{11}$, $d = (a_{exp.}/4)\sqrt{3}$, $e = (3a_{exp.}/8)\sqrt{3}$, $f = (a_{exp.}/4)\sqrt{6}$. The bond angles ($\theta_1$, $\theta_2$, $\theta_3$, $\theta_4$, $\theta_5$) were calculated using the subsequent expressions [25]. $\theta_1 = \cos^{-1}\left[(p^2 + q^2 - c^2)/2pq\right]$, $\theta_2 = \cos^{-1}\left[(p^2 + r^2 - e^2)/2pr\right]$, $\theta_3 = \cos^{-1}\left[(2p^2 - b^2)/2p^2\right]$, $\theta_4 = \cos^{-1}\left[(p^2 + s^2 - f^2)/2ps\right]$, $\theta_5 = \cos^{-1}\left[(r^2 + q^2 - d^2)/2rq\right]$. Where, (b, c, d, e, f) and (p, q, r, s) are the interionic distances between cations ($M_e$-$M_e$) and between cation and anion ($M_e$-O) respectively.

## 4. Results and discussions

Figure 1 (a) represents the X-ray diffraction (XRD) pattern of all the samples of $Zn_{0.75-x}Ni_xMg_{0.15}Cu_{0.1}Fe_2O$ (x= 0.00, 0.15, 0.30, 0.60, 0.75) spinel ferrite system. Fig. 1 (b, c) respectively

depicts the Reitveld refinement for the composition x = 0.3 and x = 0.6, done via MAUD (Material Analysis Using Diffraction) software [26]. The presence of the strong diffraction peaks in the as-burnt powder corresponding to the planes (111), (220), (311), (222), (400), (422), (511/333), (440), (533) confirms the presence of cubic spinel ferrite phase similar to JCPDS card No. 08-0234. Hence, no further sintering is required in order to obtain the desire spinel ferrite phase. The as-burnt samples are in single phase form except for x = 0.75, slight presence of $\alpha$-$Fe_2O_3$ (JCPDS card No. 87-1166) is observed as a secondary phase. Formation of a secondary phase may be ascribed to the fact that the combustion process is taking place in an oxygen-rich environment. $\alpha$-$Fe_2O_3$ phase was also observed earlier in [5, 6, 27].

The linear variation of lattice parameter with $Ni^{2+}$ substitution for various compositions is shown in figure 2. It is observed that the lattice parameter of the $Ni^{2+}$ substituted Zn-Mg-Cu ferrite decreases linearly with the increasing the doping content, attributed to the replacement of larger $Zn^{2+}$ (0.060 nm) ion by smaller $Ni^{2+}$ (0.055 nm) ion. The partial replacement of $Zn^{2+}$ by $Ni^{2+}$ ion on the tetrahedral site results in the shrinkage of the unit cell. Decrease in the lattice parameter and shift of 311 peak towards higher angle with increase in nickel concentration confirms that the doped $Ni^{2+}$ ions have incorporated into the spinel structure. The linear variation of lattice constant with the doping content obeys Vegard's law [28]. Dependence of cation distribution on the experimental lattice parameter is shown in fig. 2 inset. Lattice parameter decreases linearly with increase in $Ni^{2+}$ ion occupation at tetrahedral A site. Thus, $Ni^{2+}$ ions occupying A site are mainly responsible for the shrinkage of the crystal lattice.

Intensities of the diffracted x-ray peaks directly depends on the atomic position in the spinel unit cell while the XRD peaks position depends on the shape and size of the unit cell. A closest agreement between the observed and calculated integrated intensity ratios - $I_{400/422}$, $I_{220/400}$ (Table 1) suggest that the estimated cation distribution is in good agreement with the real distribution. The orientation degree of the hk0 ($O_{hk0}$) and 220 ($O_{220}$) plane of the as-burnt $Zn_{0.75-x}Ni_xMg_{0.15}Cu_{0.1}Fe_2O$ ferrite system is also presented in table 1. The larger values of the $O_{hk0}$ and $O_{220}$ predicts the abundance of crystallites oriented in the [hk0] and [220] direction respectively. $O_{hk0}$ value first decreases for x = 0.15 and then increases for all values of x. $O_{220}$ value decreases for all values of x,

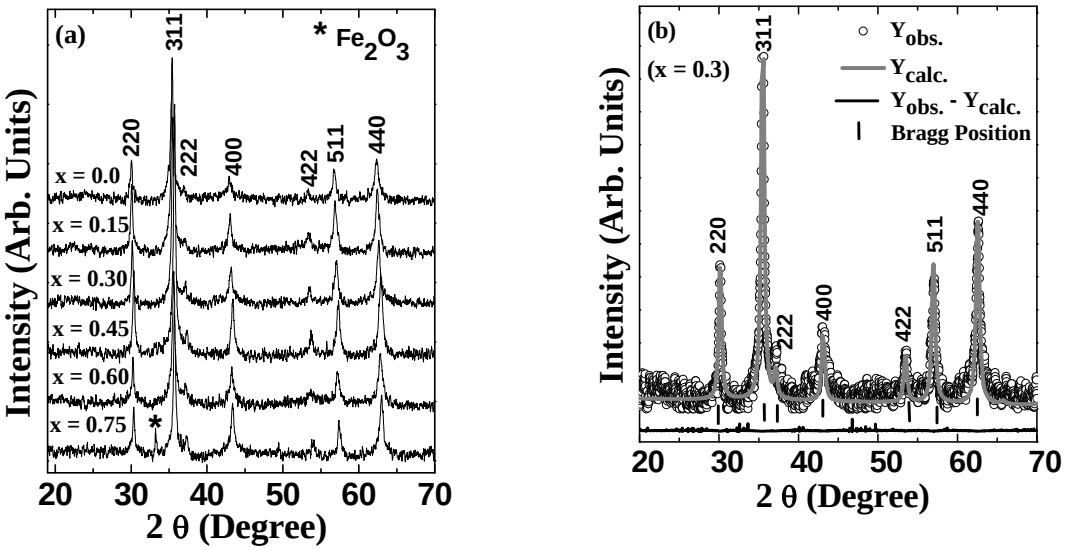


**Figure 1. (a)** XRD pattern of as-burnt $Zn_{0.75-x}Ni_xMg_{0.15}Cu_{0.1}Fe_2O_4$ system. **(b)** Reitveld refinement for the composition x = 0.3.

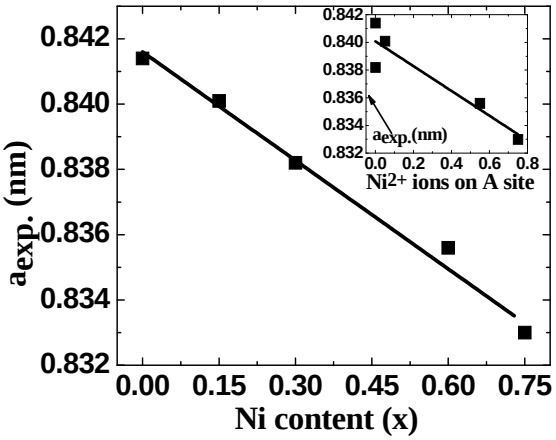


**Figure 2.** Linear decrease of experimental lattice parameter ($a_{exp.}$) with Ni doping and occupation of $Ni^{2+}$ ions at tetrahedral A site (inset).

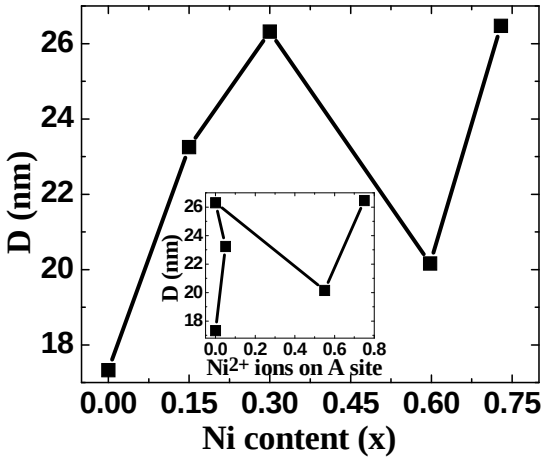


**Figure 3.** Variation of Scherrer's grain diameter (*D*) with Ni content. Inset: Dependence of *D* on $Ni^{2+}$ ion occupation at tetrahedral A site.

except for x = 0.60. The variation in the values of $O_{hk0}$ and $O_{220}$ may be ascribed to the distribution of cations at A and B site.

Figure 3 describes the variation of Scherrer's grain diameter - *D* (17.33 – 26.47 nm) with Ni (x) content. Though all the samples were prepared under identical condition, the particle size was not the same for all the $Ni^{2+}$ doped samples. D increases up to x = 0.30, decreases for x = 0.60 and again increases for x = 0.75. Such non-monotonic behavior of average crystallite size with increasing Ni concentration can be ascribed to the different dry gel formation time of the spinel ferrite, which favored the formation of new nuclei and preventing further growth of particles. It is of value to note that the highest value of D is observed for x = 0.75, which may be attributed to the presence of $Fe_2O_3$ phase [29]. Fig. 3 inset shows the particle size dependence of $Ni^{2+}$ ion occupation at tetrahedral A site. Perusal of fig. 3 shows the similar variation of particle size with Ni content and concentration of $Ni^{2+}$ ions at A site. Thus, D is mostly affected by the $Ni^{2+}$ ions occupying A site.

Table 2 displays the XRD parameters: the cell volume (*V*), hopping length at tetrahedral - A ($L_A$) and octahedral - B site ($L_B$), x-ray density ($\rho_{xrd}$) and specific surface area of the particles (*S*) of

**Table 1.** Cation distribution (for A and B site), observed, calculated intensity ratios for $I_{400/422}$, $I_{220/400}$ and orientation degree of the hk0 ($O_{hk0}$) and 220 ($O_{220}$) plane of $Zn_{0.75-x}Ni_xMg_{0.15}Cu_{0.1}Fe_2O_4$ as a function of Ni content (x).

| x | Cation distribution | $I_{400/422}$ Cal. | $I_{400/422}$ Obs. | $I_{220/400}$ Cal. | $I_{220/400}$ Obs. | $O_{hk0}$ | $O_{220}$ |
|---|---|---|---|---|---|---|---|
| 0.00 | $(Zn^{2+}_{0.75}Mg_{0.12}Cu_{0.05}Fe^{3+}_{0.08})_A$ $[Mg^{2+}_{0.03}Cu_{0.05}Fe^{3+}_{1.92}]_B$ | 1.72 | 1.76 | 1.65 | 1.65 | 0.80 | 0.39 |
| 0.15 | $(Zn^{2+}_{0.60}Ni^{2+}_{0.05}Cu_{0.05}Fe^{3+}_{0.30})_A$ $[Ni^{2+}_{0.10}Mg^{2+}_{0.15}Cu_{0.05}Fe^{3+}_{1.70}]_B$ | 1.43 | 1.41 | 1.97 | 1.65 | 0.70 | 0.36 |
| 0.30 | $(Zn^{2+}_{0.45}Fe^{3+}_{0.55})_A$ $[Ni^{2+}_{0.30}Mg^{2+}_{0.15}Cu_{0.10}Fe^{3+}_{1.45}]_B$ | 1.67 | 1.67 | 1.73 | 1.53 | 0.71 | 0.35 |
| 0.60 | $(Zn^{2+}_{0.03}Ni^{2+}_{0.55}Cu_{0.05}Fe^{3+}_{0.37})_A$ $[Zn^{2+}_{0.12}Ni^{2+}_{0.05}Mg^{2+}_{0.15}Cu_{0.05}Fe^{3+}_{1.63}]_B$ | 1.73 | 1.69 | 1.65 | 1.63 | 0.78 | 0.38 |
| 0.75 | $(Ni^{2+}_{0.75}Fe^{3+}_{0.25})_A$ $[Mg^{2+}_{0.15}Cu^{2+}_{0.10}Fe^{3+}_{1.75}]_B$ | 1.68 | 1.79 | 1.71 | 1.88 | 0.79 | 0.36 |

**Table 2.** Variation of cell volume ($V$), hopping length for A-site ($L_A$) and B-site ($L_B$), x-ray density ($\rho_{xrd}$) and specific surface area ($S$) with Ni content (x) $Zn_{0.75-x}Ni_xMg_{0.15}Cu_{0.1}Fe_2O_4$.

| x | V ($nm^3$) | $L_A$ (nm) | $L_B$ (nm) | $\rho_{xrd}$ ($Kg/m^3$) | S ($m^2/g$) |
|---|---|---|---|---|---|
| 0.00 | 0.5957 | 0.3643 | 0.2975 | 5234.32 | 66.14 |
| 0.15 | 0.5929 | 0.3638 | 0.2970 | 5236.27 | 49.28 |
| 0.30 | 0.5889 | 0.3630 | 0.2963 | 5249.42 | 43.43 |
| 0.60 | 0.5834 | 0.3618 | 0.2954 | 5253.09 | 56.66 |
| 0.75 | 0.5780 | 0.3607 | 0.2945 | 5279.47 | 42.93 |

$Zn_{0.75-x}Ni_xMg_{0.15}Cu_{0.1}Fe_2O_4$ (x = 0.00, 0.15, 0.30, 0.60, 0.75) spinel ferrite. Observed decrease in $L_A$, $L_B$ and V can be explained via replacement of an ion with higher ionic radius ($Zn^{2+}$) by an ion with lower ionic radius ($Ni^{2+}$). Decrease in the unit cell volume contribute towards the x-ray density ($\rho_{xrd}$) of Zn-Ni-Mg-Cu spinel ferrite. $\rho_{xrd}$ increases with Ni (x) content which can be attributed to the fact that the decrease in the volume of the unit cell overtakes the decrease in mass of the unit cell. Specific surface area of the as-burnt samples decreases for all values of x except for x = 0.6. High specific surface areas of particles are exceptionally essential for catalytic processes. There is an inverse relationship of particle size and density with surface area. In general, high surface areas suggest small particle sizes. The smaller is the particle size, the larger is the surface area. The catalytic property of the $Zn_{0.75-x}Ni_xMg_{0.15}Cu_{0.1}Fe_2O_4$ ferrite particles decreases with increase in Ni content.

Table 3 shows the interionic distances between cations ($M_e$-$M_e$) (*b, c, d, e, f)* for Zn-Ni-Mg-Cu as-burnt ferrite system. The observed decrease in interionic distances between cation can be can be understood by the fact that an element with higher ionic radius ($Zn^{2+}$ = 0.060 nm) is being replaced by an ion with lower ionic radius ($Ni^{2+}$ = 0.055 nm).

Figure 4 (a) illustrates the variation of the ionic radii of tetrahedral site ($r_A$) with Ni content. Decrease in $r_A$ up to x = 0.60 is due to the increase in the concentration of smaller $Fe^{3+}$ (0.049 nm) ions and decrease in the larger $Zn^{2+}$ (0.060 nm) ions on tetrahedral (A) site. Increase in $r_A$ for x = 0.75 can be attributed to the increase in the concentration of $Ni^{2+}$ (0.055 nm) ions on A site, as $Ni^{2+}$ ions migrates from octahedral (B) site to A site. Also the concentration of smaller $Fe^{3+}$ ions on A site decreases by a large amount. It is observed from fig. 4 (a, b, c, d) respectively that the ionic radii of tetrahedral site ($r_A$), oxygen positional parameter ($u$ ($\bar{4}3m$)) and distance between unshared anions ($d_{AE}$) and the tetrahedral bond length ($R_A$) varies in the same trend with Ni content (x). Variation of $u$, $d_{AE}$ and $R_A$ can be explained on the basis of $r_A$. Decrease in $r_A$ (up to x = 0.60), results in the contraction of the tetrahedral site in such a way that anions will move closer to the tetrahedrally coordinated A-site cations, which results in the decrease in oxygen positional parameter ($u$), distance between unshared anions ($d_{AE}$) and the tetrahedral bond length ($R_A$). And when $r_A$ increases with Ni content, $u$, $d_{AE}$ and $R_A$ also increases (for x = 0.75) because the tetrahedral site will expand as the anions associated with tetrahedral site move away from A-site cations. It is of value to note that the $u$ parameter value is greater than the ideal value for all the compositions of $Zn_{0.75-x}Ni_xMg_{0.15}Cu_{0.1}Fe_2O_4$. Deviation of u from its ideal value reveals distortion in the spinel structure.

Figure 5 (a) represents the variation of the ionic radii of octahedral site ($r_B$) with Ni content. With increase in Ni content $r_B$ increases up to x = 0.30 due to continues decrease in the concentration of

**Table 3.** Interionic distances between cations ($M_e$-$M_e$) (*b, c, d, e, f*) of as-burnt $Zn_{0.75-x}Ni_xMg_{0.15}Cu_{0.1}Fe_2O_4$ ferrite system.

| x | b (nm) | c (nm) | d (nm) | e (nm) | f (nm) |
|---|---|---|---|---|---|
| 0.00 | 0.2975 | 0.3488 | 0.3643 | 0.5465 | 0.5153 |
| 0.15 | 0.2970 | 0.3483 | 0.3638 | 0.5457 | 0.5145 |
| 0.30 | 0.2963 | 0.3475 | 0.3630 | 0.5444 | 0.5133 |
| 0.60 | 0.2954 | 0.3464 | 0.3618 | 0.5427 | 0.5117 |
| 0.75 | 0.2945 | 0.3453 | 0.3607 | 0.5410 | 0.5101 |

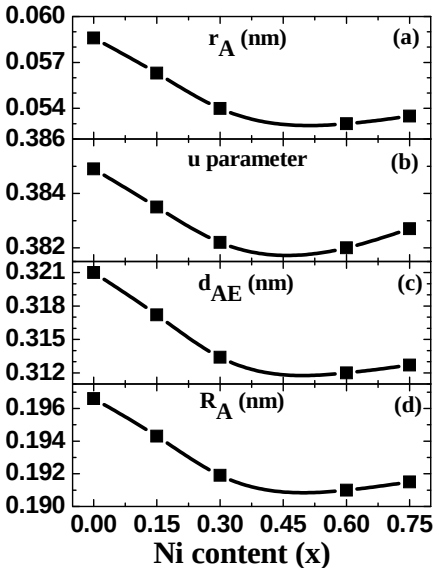


**Figure 4.** Ni content dependence of (**a**) ionic radii of A site ($r_A$), (**b**) oxygen parameter ($u$), (**c**) shared tetrahedral edge ($d_{AE}$) and (**d**) tetrahedral bond length ($R_A$) for as-burnt $Zn_{0.75-x}Ni_xMg_{0.15}Cu_{0.1}Fe_2O_4$.

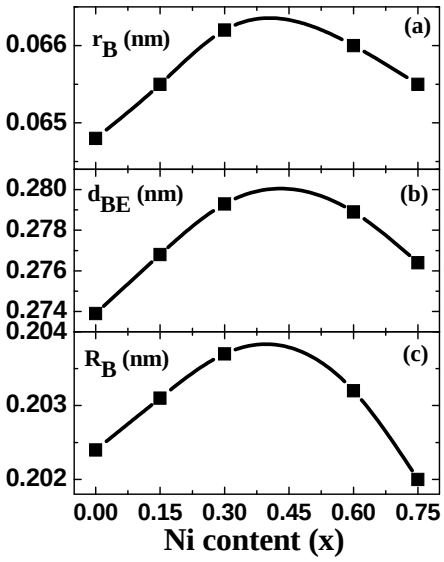


**Figure 5.** Ni content dependence of (**a**) ionic radii of B site ($r_B$), (**b**) shared octahedral edge ($d_{BE}$) and (**c**) octahedral bond length ($R_B$) for as-burnt $Zn_{0.75-x}Ni_xMg_{0.15}Cu_{0.1}Fe_2O_4$.

smaller $Fe^{3+}$ (0.0645 nm) ions and increase in the larger $Ni^{2+}$ (0.069 nm) ions on B site. Rapid decrease in $r_B$ for $x \geq 0.60$ can be ascribed to the increase in the concentration of smaller $Fe^{3+}$ ions and decrease of larger $Ni^{2+}$ ions on B site. The same variation is observed in shared octahedral edge ($d_{BE}$) and octahedral bond length ($R_B$) with Ni content as depicted in fig. 5 (b) and (c) respectively. $d_{BE}$ and $R_B$ increases up to $x = 0.30$ and decreases for $x \geq 0.60$. The variation in $d_{BE}$ and $R_B$ can be explain on the basis of ionic radii of B site. When $r_B$ increases, the anions associated with octahedral site move away from it thus, increasing the distance between octahedral cation-anion ($R_B$) and the distance between the "shared anions ($d_{BE}$). Similarly, when $r_B$ decreases, the anions associated with octahedral site will move closer to it thus, decreasing $R_B$ and $d_{BE.}$

It is of value to note that, in case of spinel ferrites XRD pattern not only gives information about structural data but, it also provides the magnetic information. One can predict the magnetic information in the form of Neel magnetic moment per unit Bohr Magneton ($n_B^N$ ($\mu_B$)) from the cation distribution (calculated as: $M_B$ - $M_A$, where $M_B$ and $M_A$ are respectively magnetic moment of B and A site) which is estimated from the x-ray diffraction intensities. Such type of magnetic information extracted from the diffraction pattern is also specified in our previous work [30].

Cation distribution parameters: oxygen positional parameter ($u$), relative bond angles ($\theta_1^{A\text{-}O\text{-}B}$, $\theta_2^{A\text{-}O\text{-}B}$, $\theta_3^{B\text{-}O\text{-}B}$, $\theta_4^{B\text{-}O\text{-}B}$, $\theta_5^{A\text{-}O\text{-}A}$) and Neel's magnetic moment affects the magnetic interaction between tetrahedral (A) and octahedral [B] site of spinel ferrite. The magnetic properties of the spinel ferrite materials originate from the spin magnetic moment of the unpaired transition-metal 3d electrons, coupled by the super-exchange interaction via oxygen ions separating the magnetic ions. The magnetic properties of ferrites are also greatly influenced by the exchange interactions. In ferrites, the exchange interaction takes place by the participation of oxygen 'anions' and is called super-exchange interaction. Since in ferrites magnetic ions occupy (A) and (B) sites, so there are three possible super-exchange interactions namely: $J_{AA}$ (A–O–A), $J_{AB}$ (A–O–B), and $J_{BB}$ (B–O–B). According to Neel's two sub lattice model of ferrimagnetism, $J_{AB} >> J_{BB}$, whereas $J_{AA}$ is small (*hence, not consider in the calculation*) due to the large separation between two A-site ions. Neel's magnetic moment (Net

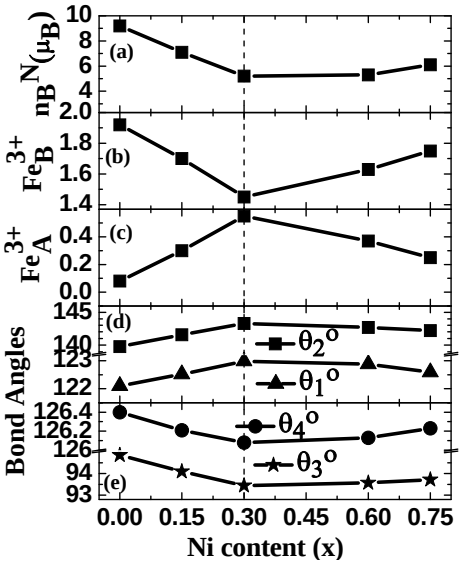


**Figure 6.** Variation of (**a**) Neel magnetic moment ($n_B^N$ ($\mu_B$)), (**b**) $Fe^{3+}$ content at tetrahedral site ($Fe^{3+}{}_A$), (**c**) $Fe^{3+}$ content at octahedral site ($Fe^{3+}{}_B$), (**d**) bond angles between A-O-B ($\theta_1$, $\theta_2$) and (**e**) bond angles between B-O-B ($\theta_3$, $\theta_4$) with Ni content (x). Dotted vertical line ( at x = 0.3 ) depicts change in the trend in the above mentioned parameters.

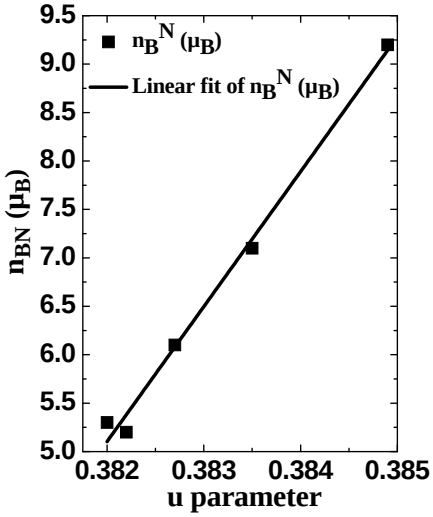


**Figure 7.** Variation of Neel magnetic moment ($n_B^N$ ($\mu_B$)) with oxygen positional parameter ($u$).

magnetic moment) of lattice is therefore, difference between the magnetic moment of B ($M_B$) and A ($M_A$) sub lattice [31]: $n_B^N = M_B - M_A$. The variation of Neel's magnetic moment with Ni (x) content is represented in fig. 6 (a). The value of Neel's magnetic moment were calculated considering the magnetic moments for $Mg^{2+}$, $Ni^{2+}$, $Zn^{2+}$, $Cu^{2+}$ and $Fe^{3+}$ - 0$\mu_B$, 2$\mu_B$, 0$\mu_B$, 1$\mu_B$ and 5$\mu_B$ respectively. Since, the magnetic moment of $Fe^{3+}$ ions is much greater than the magnetic moment of the rest of the cations ($Mg^{2+}$, $Ni^{2+}$, $Zn^{2+}$, $Cu^{2+}$) therefore, the concentration of $Fe^{3+}$ ions occupying A and B site are mainly responsible for Neel's magnetic moment. $Fe^{3+}$ concentration at B ($Fe^{3+}{}_B$) and A ($Fe^{3+}{}_A$) is also depicted in fig. 6 (b,c). $n_B^N$ decreases up to x = 0.3 because of the decrease in the magnetic moment at B site ($M_B$) and increase in the magnetic moment at A site ($M_A$) and hence, the net magnetic moment ($M_B$-$M_A$) decreases. The magnetic moment at B site decreases due to decrease in the $Fe^{3+}$ concentration at B site. Increase in $Fe^{3+}$ content on A site, increases the magnetic moment at A site. Similarly, $n_B^N$ increases for x ≥ 0.60 because of increase in the magnetic moment at B site (as $Fe^{3+}$ at B site increases) and decrease in the magnetic moment at A site (as $Fe^{3+}$ at A site decreases) and hence, the magnetic moment decreases. Figure 6 (d) also illustrates the variation of the bond angles $\theta_1$, $\theta_2$ with Ni content (x). The bond angles $\theta_1$, $\theta_2$ are the angles between A-O-B. The bond angles $\theta_1$, $\theta_2$ initially increases up to x = 0.3 and thereafter, decreases up to x = 0.75. Increase in the bond angles $\theta_1$, $\theta_2$ suggests strengthening of A-B interaction (for 0 < x ≤ 0.3) and decrease in the bond angles $\theta_1$, $\theta_2$ indicate weakening of A-B interaction (for 0.3 < x ≤ 0.75). Similarly, the variation of the bond angle between B-O-B ($\theta_3$, $\theta_4$) is depicted in fig. 6 (e). Perusal of fig. 6 (e) shows that the bond angles $\theta_3$, $\theta_4$ initially decreases up to x = 0.3, and increases up to x = 0.75. Increase in the bond angles $\theta_3$, $\theta_4$ indicate strengthening of B-B interaction (for 0 < x ≤ 0.3) and decrease in $\theta_3$, $\theta_4$ suggests weakening of B-B interaction (for 0.3 < x ≤ 0.75). The variation of the bond angles: $\theta_1$, $\theta_2$, $\theta_3$, $\theta_4$ with Ni content are consistent with that of Neel magnetic moment. Due to decrease in $Fe^{3+}$ ions at B site up to x = 0.3, B-B-interaction decreases ($\theta_3$, $\theta_4$ decreases) and A- B interaction increases ($\theta_1$, $\theta_2$ increases) which in turn decreases the Neel magnetic moment and for 0.3 < x ≤ 0.75, B-B-interaction increases ($\theta_3$, $\theta_4$ increases) and A- B interaction decreases ($\theta_1$, $\theta_2$ decreases) which in turn increases the Neel magnetic

moment. Thus increase/decrease in B-B interaction is responsible for increase/decrease in Neel magnetic moment.

Neel's magnetic moment also depends on the oxygen positional parameter ($u$). Whenever distortion is created in the crystal, cation redistribution occurs at A and B site, which alters the magnetic moment of A and B site. Fig. 7 shows a linear increase in oxygen positional parameter ($u$) with Neel's magnetic moment. As u parameter increases distortion is created in the spinel structure which forces more $Fe^{3+}$ ions to remain on B site, contributing in the enhancement of magnetic moment.

## 5. Summary

$Zn_{0.75-x}Ni_xMg_{0.15}Cu_{0.1}Fe_2O_4$ with x = 0.0, 0.15, 0.30, 0.60, 0.75 ferrites were synthesized by sol-gel auto-combustion technique without any heat treatment. X-ray diffraction analysis confirms the cubic spinel phase formation with a secondary phase of $Fe_2O_3$ for x = 0.75. Broadness of the diffraction peaks (311) indicates smaller particle formation. With increase in Ni content catalytic property of the $Zn_{0.75-x}Ni_xMg_{0.15}Cu_{0.1}Fe_2O_4$ ferrite particles decreases because of the decrease in specific surface area of the particles. The lattice parameter decreases linearly with Ni content and follows Vegard's law in the entire studied range of composition. Other structural parameters - unit cell volume ($V$), hopping length at A ($L_A$) and B site ($L_B$), x-ray density ($\rho_{XRD}$) decreases with increase in Ni content. Close occurrence between calculated and observed intensities ratio shows that the estimated cation distribution is in good agreement with the actual one. The interionic distances between cations ($M_e$-$M_e$) (*b, c, d, e, f)* decreases with Ni substitution. The migration of cations between A and B site bring perceptible changes in theoretical lattice parameter ($a_{th.}$), ionic radii of A-site ($r_A$) and B-site ($r_B$), oxygen positional parameter ($u$), shared tetrahedral and octahedral edge ($d_{AE}$, $d_{BE}$). Magnetic information in the form of Neel magnetic moment ($n_B^N$) is also extracted with the help of structural data. The B-B interaction is responsible for the variation of Neel magnetic moment with Ni content (x).

## Acknowledgments

This work is supported by MPCST project No.1783/CST/R & D/Phy and, Engg Sc and by UGC-DAE CSR, Indore [CSR-IC/CRS-74/2014-15/2104]. Authors thank Dr. M. Gupta, UGC-DAE CSR, Indore for XRD measurements.

## References

[1] Zhang J, Shi J and Gong M 2009 *J. Solid State Chem.* **182** 2135
[2] Gao X, Du Y, Liu X, Xu P and Han X 20111 *Mater. Res. Bull.* **46** 643
[3] Gabal M A and Al Angari Y M 2010 *J. Magn. Magn. Mater.* **322** 3159
[4] Yue Z, Guo W, Zhou J, Gui Z and Li L 2004 *J. Magn. Magn. Mater.* **270** 216
[5] Ghosh A, Satalkar M, Rathod S, Nag S P, Vyas P, Kane S N, Ghodke N, Prasad R and Dwivedi R, *International J. of Modern Physics: Conf. Series* **22** (2013) 28
[6] Satalkar M, Kane S N, A. Ghosh, N. Ghodke, G. Barrera, F. Celegato, M. Coisson, P. Tiberto, F. Vinai 2014 *J. Alloys Comp.* **615** S313
[7] Sun S, Zeng H, Robinson D B, Raoux S, Rice P M, Wang S X and Li G 2004 *J. Am. Chem. Soc.* **126** 273
[8] Chen Q and Zhang Z J 1998 *Appl. Phys. Lett.* **73** 3156
[9] Niu X, Du W and Du W 2004 *Sensor Actuators B* **99** 405
[10] Costa A C F M, Lula R T, Kiminami R H G A, Gama L F V, de Jesus A A and Andrade H M C 2006 *J. Mater. Sci.* **41** 4871
[11] Kobayashi M, Shirai H and Nunokawa M 2002 *Ind. Eng. Chem. Res.* **41** 2903
[12] Dey S, Dey S K, Ghosh B, Reddy V R and Kumar S 2013 *Mater. Chem. Phys.* **138** 833
[13] Zhang H, Ma Z, J.Zhou, Z. Yue, L. Li and Z. Gui 2000 *J. Magn. Magn. Mater.* **213** 304

[14] Bachhava S G, Patil R S, Ahirrao P B, Patil A M and Patil D R 2011 *Mater. Chem. Phys.* **129** 1104
[15] Chinnasamy C N, Yang A, Yoon S D, Hsu K, Shultz M D, Carpenter E E, Mukerjee S, Vittoria C and Harris V G 2007 *J. Appl. Phys.* **101** 09M509
[16] Smit J and Wijn H P J 1959 *Ferites* (Eindhoven, The Netherlands: Philips Technical Library)
[17] Cullity B D 1978 *Elements of X-ray diffraction* (Philippines: Addison-Wesley Publishing Co.)
[18] Amer M A and Hiti M L 2001 *J. Magn. Magn. Mater.* **234** 118
[19] Qi X, Zhou J, Yue Z, Gui Z and Li L 2003 *Mater. Sc. and Eng. B* **99** 278
[20] Weil L, Bertaut E F and Bochirol L 1950 *J. Phys. Radium* **11** 208
[21] Tanna A R and Joshi H H 2013 *World Academy of Sc. And Eng. Tech.* **75** 334
[22] Schwartz R W, Clem P G, Voigt J A, Byhoff E R, Stry M V, Headley T J and Missert N A 1999 *J. Am. Ceram. Soc.* **82** 2359
[23] Lakhani V K, Pathak T K, Vasoya N H and Modi K B 2011 *Solid State Sc.* **13** 539
[24] Shannon R D 1976 *Acta Cryst* **A32** 751
[25] Sickafus K E, Wills J M and Grimes N W 1999 *J. Am. Ceram. Soc.* **82** 3279
[26] Lutterotti L and Scardi P 1990 *J Appl Cryst* **23** 246
[27] López J G, Rodriguez-Senín E, Pastor J Y, Paris M A, Martín A, Levenfeld B and Várez A 2011 *Powder Technology* **210** 29
[28] Vegard L 1969 *Zeitscchrift fur Physik* **5** 17
[29] Sun K, Zhongwen L, Zhong Y, Xiona J and Jiaomin H 2011 *J. Magn. Magn. Mater.* **323** 927
[30] Satalkar M, Kane S N, Kulriya P K and Avasthi D K 2016 *Nucl. Instrum. Methods B* **379** 235
[31] Gadkari A B, Shinde T J and Vasambekar P N 2010 *J. Magn. Magn. Mater.* **322** 3823